Three-Dimensional Kinematics of the Rheumatoid Wrist After Partial Arthrodesis

By Sayuri Arimitsu, MD, Tsuyoshi Murase, MD, PhD, Jun Hashimoto, MD, PhD, Hideki Yoshikawa, MD, PhD, Kazuomi Sugamoto, MD, PhD, and Hisao Moritomo, MD, PhD

Investigation performed at the Department of Orthopaedic Surgery, Osaka University, Osaka, Japan

Background: Partial arthrodesis of the wrist, such as radiolunate and radioscapholunate arthrodesis, is intuitively more appealing for the treatment of the rheumatoid wrist than total arthrodesis is because it preserves some motion. However, wrist kinematics after partial arthrodesis are incompletely understood. The purpose of the present study was to evaluate the kinematics of the radiocarpal and midcarpal joints of rheumatoid wrists with use of three-dimensional computed tomography before and after partial arthrodesis.

Methods: We selected ten wrists that were affected by rheumatoid arthritis in which the radiolunate joint was severely damaged but the midcarpal joint congruities were relatively well preserved. Six radiolunate and four radioscapholunate arthrodeses were then performed, with preservation of the joint congruity between the scaphoid, lunate, and capitate. We acquired in vivo three-dimensional kinematic data during wrist flexion-extension preoperatively and postoperatively with use of computed tomography and a markerless bone-registration technique. Postoperative midcarpal joint congruity and range of motion were compared with preoperative values.

Results: The mean range of global wrist motion was 48° ± 21° after radiolunate arthrodesis and 47° ± 14° after radioscapholunate arthrodesis. Midcarpal joint congruities and motion between the scaphoid, lunate, and capitate were well preserved in all ten wrists. The postoperative range of capitate motion relative to the lunate was 109% of the preoperative value after radiolunate arthrodesis and 88% after radioscapholunate arthrodesis. The directions of capitate motion relative to the lunate after both types of partial arthrodesis were significantly more oblique than before the arthrodeses, changing from radiodorsal to ulnopalmar along the so-called dart-throwing motion plane ($p < 0.05$).

Conclusions: The results of this kinematic analysis, which showed that midcarpal motion occurred in the dart-throwing motion plane, may support the use of radiolunate and radioscapholunate arthrodeses as an alternative to total wrist arthrodesis in patients with symptomatic rheumatoid arthritis of the wrist.

Level of Evidence: Therapeutic Level IV. See Instructions to Authors for a complete description of levels of evidence.

The aim of the surgical treatment of the wrist that is affected by rheumatoid arthritis is to achieve a painless, stable, and functional joint[1]. Total wrist arthrodesis has been used in severe cases in which there is collapse of both the radiocarpal and midcarpal articulations. A high fusion rate and good pain relief can be expected, but many patients find the loss of motion to be limiting[2]. In a painful wrist with destruction of the radiocarpal joint and an intact midcarpal joint, preservation of partial motion is a worthwhile goal[2]. Partial arthrodesis of the wrist, such as radiolunate or radioscapholunate arthrodesis, might be preferable. The choice between total and partial arthrodesis is usually decided on the basis of radiographs alone. However, a recent three-dimensional study revealed that the midcarpal motion of wrists with rheumatoid arthritis was better preserved than previously thought and suggested a more positive view of the utility of partial arthrodesis[3].

Radiolunate arthrodesis is a well-established procedure, and several researchers have reported successful clinical results in association with this operation[1,4-12]. It has been suggested that radiolunate arthrodesis is most useful for the treatment of

Disclosure: In support of their research for or preparation of this work, one or more of the authors received, in any one year, outside funding or grants of less than $10,000 from the Nakatani Foundation of Electronic Measuring Technology Advancement. Neither they nor a member of their immediate families received payments or other benefits or a commitment or agreement to provide such benefits from a commercial entity. No commercial entity paid or directed, or agreed to pay or direct, any benefits to any research fund, foundation, division, center, clinical practice, or other charitable or nonprofit organization with which the authors, or a member of their immediate families, are affiliated or associated.

rheumatoid arthritis in patients in whom the disease has left the midcarpal and radioscaphoid joints relatively unaffected. Radioscapholunate arthrodesis has been found to be useful for patients in whom the entire radiocarpal joint has been destroyed or dislocated but the midcarpal joint is preserved[2,13]. However, some researchers have reported a marked decrease in the range of motion after radioscapholunate arthrodesis[4]. The wrist kinematics after a partial arthrodesis are incompletely understood.

Recently, researchers have been able to measure the three-dimensional kinematics of human joints in vivo with use of a markerless bone-registration technique, which provides three-dimensional views of bones and allows for the evaluation of their precise range and direction of motion by determining the relative positions of the bones in different volume images[3,14-20]. The purpose of the present study was to evaluate the kinematics of the radiocarpal and midcarpal joints of rheumatoid wrists with use of three-dimensional computed tomography before and after radiolunate and radioscapholunate arthrodesis.

Materials and Methods

Subjects

We acquired in vivo kinematic data by means of three-dimensional computed tomography in order to investigate the pathological condition of forty-two wrists in thirty-seven patients with rheumatoid arthritis who had continuous wrist pain, instability, and/or extensor tendon rupture. We assessed the suitability of the midcarpal joint for partial arthrodesis by means of three-dimensional computed tomographic images with use of a bone surface model made with the wrist in a neutral position.

In eighteen of the forty-two wrists, the midcarpal joint was found to be well preserved. Eight of these eighteen wrists were in patients who elected not to have surgery or dropped out of the study. The remaining ten wrists were selected for partial arthrodesis; all had severe radiolunate damage, but all had a relatively well-preserved and congruent midcarpal joint. All patients were female, and the average age was fifty-eight years (range, twenty-three to seventy-one years). The average duration of rheumatoid arthritis was eleven years (range, five to seventeen years), and the average interval between surgery and postoperative image acquisition was nineteen months (range, five to forty-two months).

A radiolunate arthrodesis was used in six wrists; all had a severely damaged radiolunate joint but a normal radioscaphoid articulation. A radioscapholunate arthrodesis was chosen for four wrists in which destruction and subluxation or dislocation of the radioscaphoid joint were detected on direct intraoperative observation. All subjects consented to participate in the present study.

Surgical Technique

All of the procedures were performed by two specialists in hand surgery (H.M. and T.M.), who are the senior authors of the present study. The wrist joint was approached through a dorsal midline skin incision. The dorsal compartments were separated and elevated radially from the radius. In addition, we performed tendon transfer in three wrists, synovectomy in all ten wrists, hemiresection of the ulnar head in seven wrists, and a Darrach procedure in three wrists. The capsule of the radiocarpal and distal radioulnar joints was opened, and synovectomy, hemiresection of the ulnar head, and/or a Darrach procedure was performed as appropriate. The articular surfaces of the scaphoid, lunate, and radius were exposed, and the damaged articular cartilage and cortical bone were removed. For bone graft, we used cancellous bone harvested from the iliac crest in five of the ten wrists and the excised ulnar head in all ten wrists. For fixation, three or four Kirschner wires were used in six wrists and two Kirschner wires with a staple were used in four wrists. For radiolunate arthrodesis, the lunate was fixed in the neutral position with use of enough bone graft to restore height and to keep the distal surfaces of the scaphoid and lunate precisely aligned to produce smooth midcarpal motion with good congruity of the distal surfaces of the scaphoid and lunate. For radioscapholunate arthrodesis, the scaphoid and lunate were each positioned with a temporary Kirschner wire, which was used as a joystick. The scaphoid and the lunate were carefully aligned to the neutral position by fitting each to the proximal articular surface of the capitate. The average flexion of the lunate and scaphoid with respect to the longitudinal axis of the radius measured 51° ± 7° and 5° ± 4°, respectively, consistent with the natural posture as previously reported[21]. The decision to perform a radiolunate or radioscapholunate arthrodesis was made after direct observation of the cartilage status and the congruity of the radioscaphoid joint.

Postoperative immobilization involved the use of a long arm cast for approximately three weeks, followed by a removable splint for two weeks. The patients were able to perform active motion of the wrist and forearm four weeks after the operation. Complete osseous union was achieved in all patients within three months.

Image Acquisition

The technique that we used for in vivo three-dimensional kinematic evaluation has been described in detail previously[3,15-20]. We performed three-dimensional computed tomography on the wrists preoperatively and postoperatively with use of a clinical helical-type scanner with an image slice thickness of 0.625 mm (LightSpeed XTra; GE Healthcare, Waukesha, Wisconsin). We made images with the wrist in three different positions: neutral (in which the third metacarpal and the forearm axis were aligned), maximum wrist flexion, and maximum wrist extension. Data were saved in a standard format (Digital Imaging and Communications in Medicine) that is used commonly for transferring and storing medical images.

Segmentation and Registration

Regions of individual bones were segmented semi-automatically with use of a software program for image analysis (Virtual

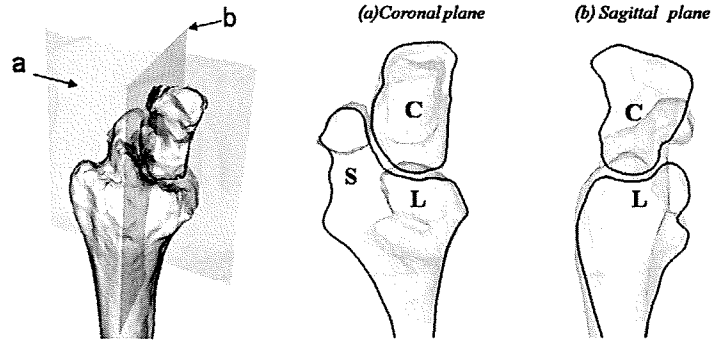

Fig. 1

Illustrations depicting the method used to evaluate midcarpal joint congruity after radiolunate or radioscapholunate arthrodesis. We qualitatively evaluated joint congruity by means of three-dimensional investigation of the bone surface models from any direction and on any cutting plane with use of specially developed software. S = scaphoid, L = lunate, and C = capitate.

Place-M; AZE, Tokyo, Japan). The software generated three-dimensional surface bone models with use of the marching cubes technique[22]. The kinematic variables were calculated by registering the segmented bones[14] from one position to another with use of the software. The accuracy of volume-based registration has been discussed previously[15].

Three-Dimensional Evaluation of Joint Congruity

The three-dimensional bone models created from computed tomography slice data could be viewed and qualitatively evaluated from any direction and on any cutting plane with use of originally developed software (Orthopedics Viewer; Osaka University, Osaka, Japan)[20]. We qualitatively evaluated joint congruity by means of three-dimensional investigation of the bone surface models with use of this software preoperatively and postoperatively (Fig. 1).

Three-Dimensional Quantification of Range of Motion

The radius and all carpal bones except the pisiform were registered, and the relative motion of each bone was calculated. In general, the displacement of the moving body from one position to another can always be represented as a rotation around and translation along a unique axis, which is called a screw axis[23]. We defined this screw axis as an axis of rotation. The three-dimensional range of motion was calculated as the angle of rotation around the axis of rotation[18].

Global wrist motion during wrist flexion-extension before the radiolunate or radioscapholunate arthrodesis, which was represented by capitate motion relative to the radius, was compared with postoperative global wrist motion, represented by capitate motion relative to the fixed lunate.

Midcarpal motion during wrist flexion-extension before the arthrodesis, which was represented by capitate motion

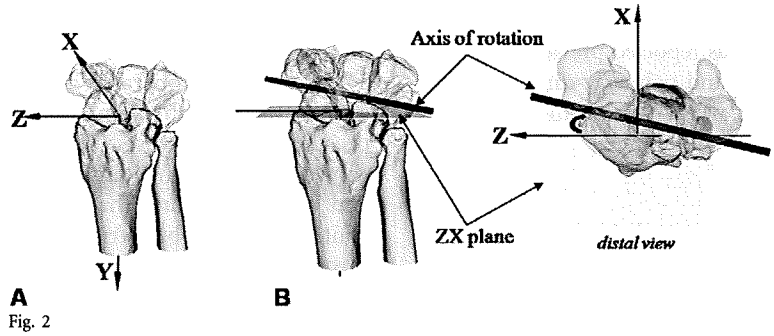

Fig. 2

Illustrations depicting the three-dimensional evaluation of the direction of motion in a wrist following radiolunate arthrodesis. *A:* Orthogonal reference system established for the radius. The Y axis was defined as the longitudinal axis of the radius, the Z axis was defined as the line running through the radial styloid process on the plane perpendicular to the Y axis, and the X axis was defined as the line perpendicular to the YZ plane. *B:* We defined the angle as a "radially and palmarly-directed opening angle" (curved arrow), which was the angle of the axis of rotation relative to the axis of wrist flexion and extension (the Z axis).

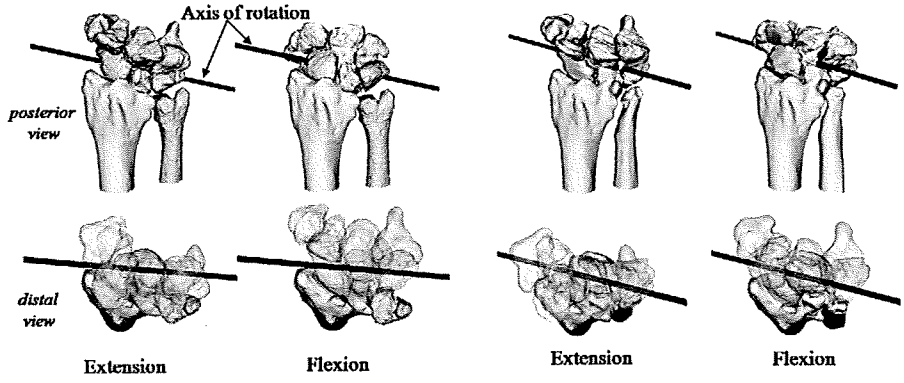

Fig. 3

Posterior and distal views of the right wrist and the axes of rotation during wrist flexion-extension motion before and after radiolunate arthrodesis. *A:* Global wrist motion before the radiolunate arthrodesis. *B:* Global wrist motion after the radiolunate arthrodesis. The postoperative direction of global wrist motion was more oblique from radiodorsal to ulnopalmar along the so-called dart-throwing motion plane as compared with the preoperative direction of global wrist motion.

relative to the scaphoid, lunate, and triquetrum, was compared with postoperative values.

We also evaluated radiocarpal and scapholunate motion preoperatively and postoperatively.

Three-Dimensional Evaluation of Direction of Motion

To quantify the three-dimensional direction of motion, we defined a grid for the radius, which was the orthogonal reference system described by Belsole et al. (Fig. 2, *A*)[24]. A consistent orthogonal reference system was established in the radius in the neutral position, as previously reported[3,25].

After determination of each axis of rotation, the angle of the axis of rotation relative to the axis of wrist flexion and extension (the Z axis of the orthogonal reference system) was calculated as viewed in the axial plane of the radius, defined as the ZX plane. We defined this angle as the radially and palmarly-directed opening angle, as reported previously (Fig. 2, *B*)[19,20]. We evaluated the radially and palmarly-directed opening angle with regard to global wrist motion and midcarpal motion.

Statistical Analysis

All data were expressed as the mean and the standard deviation. Quantitative data on the wrists before and after the operation were compared with use of standard statistical formulas based on the Mann-Whitney U test. Differences were deemed to be significant at $p < 0.05$.

Source of Funding

This research was financially supported by the Nakatani Foundation of Electronic Measuring Technology Advancement, which did not play a role in the investigation. The financial support was used for the supplies, including two computers used for analysis.

Results

Radiolunate Arthrodesis

Global Wrist Motion

The average global range of wrist motion during wrist flexion-extension was 59° ± 4° before radiolunate arthrodesis and 48° ± 21° after radiolunate arthrodesis. The postoperative value was 81% of the preoperative value, but the difference was not significant ($p = 0.34$).

The preoperative direction of global wrist motion was close to the sagittal plane, whereas the postoperative direction of global wrist motion was more oblique from radiodorsal to ulnopalmar along the so-called dart-throwing motion plane (Fig. 3). The radially and palmarly-directed opening angle was 5° ± 13° preoperatively, compared with 25° ± 10° postoperatively; this difference was significant ($p = 0.01$) (Table I).

Midcarpal Motion

The residual postoperative midcarpal motion and joint congruities between the scaphoid, lunate, and capitate were well preserved in all cases. The three-dimensional animation showed that all of the joints in the wrist were moving smoothly and congruently and that scapholunate motion appeared to contribute to global wrist motion after the radiolunate arthrodesis (see Appendix). The average preoperative ranges of capitate motion relative to the scaphoid, lunate, and triquetrum during wrist flexion-extension were 21° ± 9°, 44° ± 8°, and 36° ± 5°, respectively. After radiolunate arthrodesis, the average capitate motions relative to the scaphoid, lunate, and triquetrum were 19° ± 12°, 48° ± 21°, and 31° ± 16°, respectively. The postoperative capitate motion relative to the lunate was 109% of the preoperative value. The postoperative capitate motions relative to the scaphoid and triquetrum were slightly less than the preoperative values (90% and 87%, respectively). However, there was no significant difference in any

TABLE I Kinematic Data in Wrist Flexion-Extension Motion Before and After Radiolunate and Radioscapholunate Arthrodesis*

	Radiolunate Arthrodesis		Radioscapholunate Arthrodesis	
	Before	After	Before	After
Range of motion around axis of rotation *(deg)*				
Capitate to radius	59 ± 4	48 ± 21	83 ± 24	47 ± 14
Capitate to scaphoid	21 ± 9	19 ± 12	18 ± 7	47 ± 14
Capitate to lunate	44 ± 8	48 ± 21	53 ± 21	47 ± 14
Capitate to triquetrum	36 ± 5	31 ± 16	37 ± 14	28 ± 13
Scaphoid to lunate	30 ± 10	30 ± 15	37 ± 15	0 ± 0
Scaphoid to radius	44 ± 11	30 ± 15	66 ± 21	0 ± 0
Lunate to radius	17 ± 9	0 ± 0	31 ± 15	0 ± 0
Radially and palmarly-directed opening angle *(deg)*				
Capitate to radius	5 ± 13	25 ± 10	−2 ± 5	19 ± 11
Capitate to scaphoid	43 ± 25	41 ± 21	3 ± 15	19 ± 11
Capitate to lunate	8 ± 13	25 ± 10	2 ± 6	19 ± 11
Capitate to triquetrum	7 ± 15	24 ± 13	2 ± 3	22 ± 11
Scaphoid to lunate	5 ± 14	16 ± 8	4 ± 8	—
Scaphoid to radius	4 ± 11	16 ± 8	−2 ± 7	—
Lunate to radius	4 ± 35	—	−13 ± 6	—

*The values are given as the mean and the standard deviation.

range of motion in the midcarpal joint before as compared with after radiolunate arthrodesis ($p = 1.00$ for capitate motion relative to the lunate, $p = 0.75$ for capitate motion relative to the scaphoid, and $p = 0.75$ for capitate motion relative to the triquetrum).

The preoperative direction of capitate motion relative to the scaphoid during wrist flexion-extension was oblique from radiodorsal to ulnopalmar and the radially and palmarly-directed opening angle was 43° ± 25°, whereas the preoperative directions of capitate motion relative to the lunate and triquetrum were closer to the sagittal plane than to that of the scaphoid and the radially and palmarly-directed opening angles were 8° ± 13° and 7° ± 15°, respectively. After radiolunate arthrodesis, the direction of capitate motion relative to the scaphoid was oblique from radiodorsal to ulnopalmar, the radially and palmarly-directed opening angle was 41° ± 21°, and the directions of capitate motion relative to the lunate and triquetrum were 25° ± 10° and 24° ± 13°, respectively. The postoperative direction of capitate motion relative to the lunate was significantly more oblique than the preoperative value ($p = 0.03$). The directions of capitate motion relative to the scaphoid and triquetrum did not differ significantly before as compared with after radiolunate arthrodesis ($p = 0.63$ and 0.10, respectively) (Table I).

Radiocarpal Motion

The preoperative range of lunate motion relative to the radius was 17° ± 9°. The preoperative range of scaphoid motion relative to the radius during wrist flexion-extension was 44° ± 11°, whereas the postoperative value was 30° ± 15°. The range of scaphoid motion relative to the radius did not differ significantly before as compared with after radiolunate arthrodesis ($p = 0.11$) (Table I).

Scapholunate Motion

The preoperative range of scaphoid motion relative to the lunate during wrist flexion-extension was 30° ± 10°, whereas the postoperative value was 30° ± 15° (Table I). The difference was not significant.

Radioscapholunate Arthrodesis

Global Wrist Motion

The average preoperative and postoperative ranges of global wrist motion were 83° ± 24° and 47° ± 14°, respectively. The postoperative value was 57% of the preoperative value.

The preoperative direction of global wrist motion was close to the sagittal plane, whereas the postoperative direction of global wrist motion was more oblique from radiodorsal to ulnopalmar along the dart-throwing motion plane as compared with the preoperative direction of global wrist motion (Fig. 4). The radially and palmarly-directed opening angle was −2° ± 5° before surgery and 19° ± 11° after surgery; this difference was significant ($p = 0.02$) (Table I).

Midcarpal Motion

The residual postoperative midcarpal motion and joint congruities between the scaphoid, lunate, and capitate were well preserved in all cases (Fig. 1) (see Appendix). The average preoperative capitate motions relative to the scaphoid,

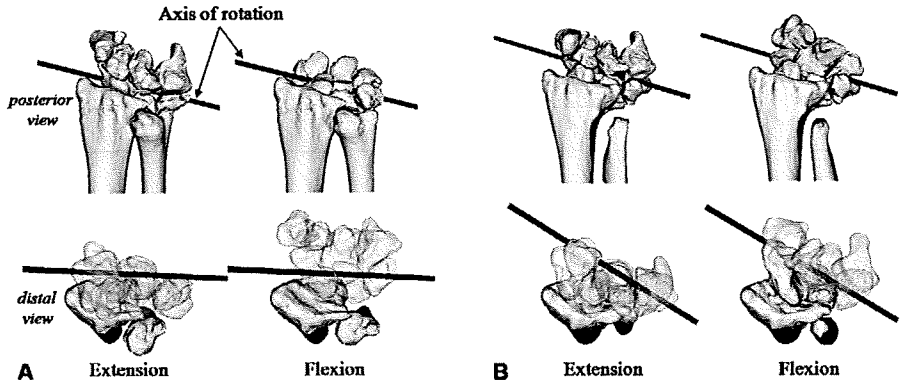

Fig. 4

Posterior and distal views of the right wrist and the axes of rotation during the wrist flexion-extension motion before and after radioscapholunate arthrodesis. *A:* Global wrist motion before radioscapholunate arthrodesis. *B:* Global wrist motion after radioscapholunate arthrodesis. The postoperative direction of global wrist motion was more oblique from radiodorsal to ulnopalmar along the so-called dart-throwing motion plane as compared with the preoperative direction of global wrist motion.

lunate, and triquetrum during wrist flexion-extension were 18° ± 7°, 53° ± 21°, and 37° ± 14°, respectively. After radioscapholunate arthrodesis, the average capitate motion relative to the lunate (with the scaphoid) and triquetrum measured 47° ± 14° and 28° ± 13°, respectively. The postoperative capitate motions relative to the lunate and triquetrum were slightly less than the preoperative motion (88% and 76% of the preoperative values, respectively). However, there was no significant difference in midcarpal motion before radioscapholunate arthrodesis as compared with after radioscapholunate arthrodesis.

The preoperative direction of capitate motion relative to the scaphoid, lunate, and triquetrum during wrist flexion-extension was almost along the sagittal plane, and the radially and palmarly-directed opening angles were 3° ± 15°, 2° ± 6°, and 2° ± 3°, respectively. After radioscapholunate arthrodesis, the direction of capitate motion relative to the lunate (with the scaphoid) and triquetrum was oblique from radiodorsal to ulnopalmar, and the radially and palmarly-directed opening angles were 19° ± 11° and 22° ± 11°, respectively. The postoperative direction of capitate motion relative to the lunate and triquetrum became significantly more oblique than the preoperative value, from radiodorsal to ulnopalmar ($p = 0.02$ and 0.02, respectively) (Table I).

Radiocarpal Motion

Before radioscapholunate arthrodesis, the radiocarpal joint was incongruent between the scaphoid, lunate, and radius during wrist flexion-extension in all cases. The preoperative ranges of scaphoid and lunate motion relative to the radius were 66° ± 21° and 31° ± 15°, respectively (Table I).

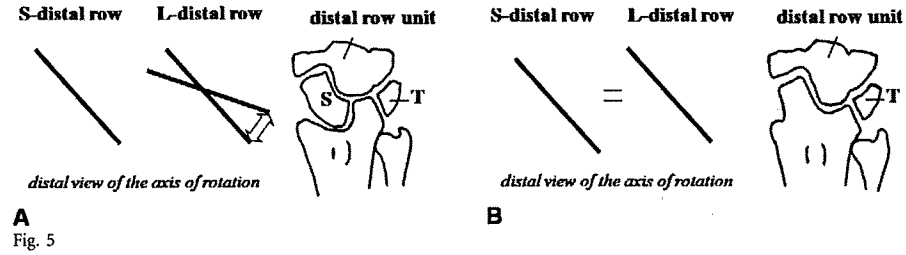

Fig. 5

Distal view of the right wrist and axes of rotation after radiolunate and radioscapholunate arthrodesis. *A:* Distal view of the axes of rotation after radiolunate arthrodesis. The direction of capitate motion relative to the scaphoid during flexion-extension was essentially uniaxial in the dart-throwing motion plane, whereas the direction of capitate motion relative to the lunate has more variability, varying from the sagittal plane to the dart-throwing motion plane. *B:* Distal view of the axes of rotation after radioscapholunate arthrodesis. The residual motion plane of the capitate after radioscapholunate arthrodesis is essentially limited to the dart-throwing motion plane. S = scaphoid, L = lunate, and T = triquetrum.

Discussion

In the present study, the preoperative midcarpal motions were well preserved after both radiolunate and radioscapholunate arthrodesis, and the ranges of capitate motion relative to the lunate were well preserved. The residual postoperative range of global wrist motion was 48° after radiolunate arthrodesis and 47° after radioscapholunate arthrodesis. The motion after radiolunate arthrodesis was 81% of the preoperative value, which was higher than the value of 68% (with the range of motion changing from 57° preoperatively to 39° postoperatively) that had been previously reported[4]. The postoperative range of global wrist motion after radioscapholunate arthrodesis was better than the range of 26° as reported in a previous study[4]. However, the postoperative range of global wrist motion (47°) after radioscapholunate arthrodesis in the present study was only 57% of the preoperative value (83°), which was greater than the preoperative value for wrists treated with radiolunate arthrodesis (59°). We speculate that the greater preoperative global range of motion in the radioscapholunate arthrodesis group was due to the difference in the type of rheumatoid disease. The wrists that were treated with radioscapholunate arthrodesis were of the unstable type[3], with ligamentous laxity, whereas the wrists that received radiolunate arthrodesis were of the stable type[3]. We think that, in unstable wrists, the radiocarpal joint was lax and usually was dislocated and that this may have provided relatively more motion than in stable wrists.

The postoperative direction of wrist motion in the present study was oblique from radiodorsal to ulnopalmar. A recent three-dimensional study revealed that capitate motion relative to the scaphoid was essentially uniaxial and that the motion plane was oblique with respect to the pure flexion-extension plane (the so-called dart-throwing motion plane), whereas the direction of capitate motion relative to the lunate had more flexibility and could range between the pure flexion-extension plane and the dart-throwing motion plane (Fig. 5, *A*)[20]. If the scaphoid is fixed to the lunate, the direction of capitate motion relative to the lunate is dominated by the direction of capitate motion relative to the scaphoid. Therefore, the residual motion plane of the capitate after radioscapholunate arthrodesis is almost limited to the dart-throwing motion plane (Fig. 5, *B*). In addition, if the lunate were fixed in an extended position relative to the scaphoid, even if their joint surfaces were to fit, the scapholunocapitate joint would be locked and smooth midcarpal motion would not be obtained. In the present study, we found a difference between radiolunate and radioscapholunate arthrodesis in terms of the postoperative radially and palmarly-directed opening angle. It has been reported that some carpal supination deformity exists in rheumatoid wrists, especially unstable-type rheumatoid wrists[3,26]. We assume that more carpal supination might remain in wrists treated with radioscapholunate arthrodesis as compared with wrists treated with radiolunate arthrodesis.

The present study had some limitations. We used three-dimensional computed tomography to evaluate joint congruity to ensure that a suitable preoperative condition was set up. However, it is not feasible for all practitioners to obtain a preoperative three-dimensional evaluation of joint congruity. We would suggest that it is important for practitioners to choose carefully the type of surgery based on the preoperative investigation and the direct intraoperative observation focusing on the cartilage preservation and the congruity of the midcarpal and radiocarpal joints. The second limitation is that the present study included only ten wrists—a sample of convenience—and such a small series does not have enough power for the detection of significant differences. We were unable to compare the outcomes of radiolunate and radioscapholunate arthrodesis in terms of patient background information such as the history of disease. The third limitation was that we examined only static three-dimensional views of the carpal bones in a limited number of wrist positions. Static measurements do not reveal functional effects that might occur during actual wrist motion. Garcia-Elias et al. reported that radioscapholunate arthrodesis and distal scaphoid excision provided significantly better results than did radioscapholunate arthrodesis alone in terms of residual pain and the decrease in radial deviation and flexion of the wrist[27]. Adding distal scaphoid excision may lead to kinematics different from those discussed here.

However, in the present study, we found that, after radiolunate and radioscapholunate arthrodesis, midcarpal motion in the dart-throwing motion plane was better preserved than was previously thought. Previous in vivo three-dimensional studies of normal wrist motion have shown that the midcarpal joint essentially moves in the plane of the dart-throwing motion, which is thought to be used frequently in the performance of many activities of daily living[20,28,29]. This may support the use of radiolunate or radioscapholunate arthrodesis as an alternative to total wrist arthrodesis in patients with rheumatoid arthritis.

Appendix

(eA) Videos demonstrating midcarpal motion and joint incongruities after a radiolunate and a radioscapholunate arthrodesis are available with the electronic versions of this article, on our web site at jbjs.org (go to the article citation and click on "Supplementary Material"). ■

NOTE: The authors thank Akira Goto, MD, PhD, Kunihiro Oka, MD, PhD, and Ryoji Nakao, computer programmer, Department of Orthopaedic Surgery, Osaka University, for assistance during parts of the experimental procedure.

Sayuri Arimitsu, MD
Tsuyoshi Murase, MD, PhD
Jun Hashimoto, MD, PhD
Hideki Yoshikawa, MD, PhD
Kazuomi Sugamoto, MD, PhD
Hisao Moritomo, MD, PhD
Department of Orthopaedic Surgery, Osaka University,
2-2 Yamadaoka, Suita-shi,
Osaka 565-0871, Japan.
E-mail address for H. Moritomo: moritomo@ort.med.osaka-u.ac.jp

References

1. Honkanen PB, Mäkelä S, Konttinen YT, Lehto MU. Radiocarpal arthrodesis in the treatment of the rheumatoid wrist. A prospective midterm follow-up. J Hand Surg Eur Vol. 2007;32:368-76.

2. Murray PM. Radioscapholunate arthrodesis. Hand Clin. 2005;21:561-6.

3. Arimitsu S, Sugamoto K, Hashimoto J, Murase T, Yoshikawa H, Moritomo H. Analysis of radiocarpal and midcarpal motion in stable and unstable rheumatoid wrists using 3-dimensional computed tomography. J Hand Surg Am. 2009;33:189-97.

4. Ishikawa H, Murasawa A, Nakazono K. Long-term follow-up study of radiocarpal arthrodesis for the rheumatoid wrist. J Hand Surg Am. 2005;30:658-66.

5. Chamay A, Della Santa D, Vilaseca A. Radiolunate arthrodesis. Factor of stability for the rheumatoid wrist. Ann Chir Main. 1983;2:5-17.

6. Linscheid RL, Dobyns JH. Radiolunate arthrodesis. J Hand Surg Am. 1985;10(6 Pt 1):821-9.

7. Stanley JK, Boot DA. Radio-lunate arthrodesis. J Hand Surg Br. 1989;14:283-7.

8. Ishikawa H, Hanyu T, Saito H, Takahashi H. Limited arthrodesis for the rheumatoid wrist. J Hand Surg Am. 1992;17:1103-9.

9. Della Santa D, Chamay A. Radiological evolution of the rheumatoid wrist after radio-lunate arthrodesis. J Hand Surg Br. 1995;20:146-54.

10. Halikis MN, Colello-Abraham K, Taleisnik J. Radiolunate fusion. The forgotten partial arthrodesis. Clin Orthop Relat Res. 1997;341:30-5.

11. Doets HC, Raven EEJ. A procedure for stabilising and preserving mobility in the arthritic wrist. J Bone Joint Surg Br. 1999;81:1013-6.

12. Borisch N, Haussmann P. Radiolunate arthrodesis in the rheumatoid wrist: a retrospective clinical and radiological longterm follow-up. J Hand Surg Br. 2002;27:61-72.

13. Simmen BR, Huber H. The rheumatoid wrist: a new classification related to the type of the natural course and its consequences for surgical therapy. In: Simmen BR, Hagena F, editors. The wrist in rheumatoid arthritis. Basel: Karger; 1992. p 13-25.

14. Besl PJ, Mackay N. A method for registration of 3-D shapes. IEEE Trans Patt Anal. 1992;14:239-56.

15. Goto A, Moritomo H, Murase T, Oka K, Sugamoto K, Arimura T, Masumoto J, Tamura S, Yoshikawa H, Ochi T. In vivo three-dimensional wrist motion analysis using magnetic resonance imaging and volume-based registration. J Orthop Res. 2005;23:750-6.

16. Oka K, Moritomo H, Murase T, Goto A, Sugamoto K, Yoshikawa H. Patterns of carpal deformity in scaphoid nonunion: a 3-dimensional and quantitative analysis. J Hand Surg Am. 2005;30:1136-44.

17. Oka K, Doi K, Suzuki K, Murase T, Goto A, Yoshikawa H, Sugamoto K, Moritomo H. In vivo three-dimensional motion analysis of the forearm with radioulnar synostosis treated by the Kanaya procedure. J Orthop Res. 2006;24:1028-35.

18. Moritomo H, Goto A, Sato Y, Sugamoto K, Murase T, Yoshikawa H. The triquetrum-hamate joint: an anatomic and in vivo three-dimensional kinematic study. J Hand Surg Am. 2003;28:797-805.

19. Moritomo H, Murase T, Goto A, Oka K, Sugamoto K, Yoshikawa H. Capitate-based kinematics of the midcarpal joint during wrist radioulnar deviation: an in vivo three-dimensional motion analysis. J Hand Surg Am. 2004;29:668-75.

20. Moritomo H, Murase T, Goto A, Oka K, Sugamoto K, Yoshikawa H. In vivo three-dimensional kinematics of the midcarpal joint of the wrist. J Bone Joint Surg Am. 2006;88:611-21.

21. Larsen CF, Mathiesen FK, Lindequist S. Measurements of carpal bone angles on lateral wrist radiographs. J Hand Surg Am. 1991;16:888-93.

22. Lorensen WE, Cline HE. Marching cubes: a high resolution 3D surface construction algorithm. Computer Graphics. 1987;21:163-9.

23. Kinzel GL, Hall AS Jr, Hillberry BM. Measurement of the total motion between two body segments. I. Analytical development. J Biomech. 1972;5:93-105.

24. Belsole RJ, Hilbelink DR, Llewellyn JA, Dale M, Ogden JA. Carpal orientation from computed reference axes. J Hand Surg Am. 1991;16:82-90.

25. Arimitsu S, Murase T, Hashimoto J, Oka K, Sugamoto K, Yoshikawa H, Moritomo H. A three-dimensional quantitative analysis of carpal deformity in rheumatoid wrists. J Bone Joint Surg Br. 2007;89:490-4.

26. Shapiro JS. The wrist in rheumatoid arthritis. Hand Clin. 1996;12:477-98.

27. Garcia-Elias M, Lluch A, Ferreres A, Papini-Zorli I, Rahimtoola ZO. Treatment of radiocarpal degenerative osteoarthritis by radioscapholunate arthrodesis and distal scaphoidectomy. J Hand Surg Am. 2005;30:8-15.

28. Li ZM, Kuxhaus L, Fisk JA, Christophel TH. Coupling between wrist flexion-extension and radial-ulnar deviation. Clin Biomech (Bristol, Avon). 2005;20:177-83.

29. Palmer AK, Werner FW, Murphy D, Glisson R. Functional wrist motion: a biomechanical study. J Hand Surg Am. 1985;10:39-46.

THE INTERNATIONAL JOURNAL OF MEDICAL ROBOTICS AND COMPUTER ASSISTED SURGERY
Int J Med Robotics Comput Assist Surg 2009; **5**: 452–457.
Published online 1 September 2009 in Wiley InterScience (www.interscience.wiley.com). **DOI:** 10.1002/rcs.277

ORIGINAL ARTICLE

Accuracy analysis of three-dimensional bone surface models of the forearm constructed from multidetector computed tomography data

Kunihiro Oka[1]*
Tsuyoshi Murase[1]
Hisao Moritomo[1]
Akira Goto[1]
Kazuomi Sugamoto[2]
Hideki Yoshikawa[1]

[1]*Department of Orthopaedic Surgery, Osaka University Graduate School of Medicine, Japan*

[2]*Department of Orthopaedic Biomaterial Science, Osaka University Graduate School of Medicine, Japan*

*Correspondence to: Kunihiro Oka, Department of Orthopaedic Surgery, Osaka University Graduate School of Medicine, 2-2 Yamada-oka, Suita, Osaka 565-0871, Japan. E-mail: oka-kunihiro@umin.ac.jp

Accepted: 6 July 2009

Abstract

Background We developed an original computer program that simulates upper limb reconstruction surgery using three-dimensional (3D) bone models constructed from computed tomography (CT) data. However, the accuracy of a bone model has not been clarified, and radiation exposure from CT scanning posed a concern. The purpose of this study was to investigate the appropriate CT parameters required to reduce radiation exposure while maintaining the accuracy of 3D models of the forearm bones.

Methods Twelve dry forearm bones were used to investigate the accuracy of 3D bone models created from two different CT parameters. The accuracy was evaluated by measuring: (a) the discrepancy between the models constructed from low- and normal-dose CT parameters; (b) the error between actual surface data derived by a contact-type coordinate measuring machine and a 3D bone model; and (c) the difference between a 3D bone model constructed from a bare dry bone and a model constructed from the same bone embedded in a radio-opaque soft tissue substitute. CT dose index (CTDI) and dose-length product (DLP) were recorded to evaluate the radiation exposure.

Results The mean error between bone models constructed from two different CT parameters was 0.04 mm. CTDI and DLP for the normal-radiation dose condition were 9.3 and 563 mGy/cm and those for the low-radiation dose condition were 0.3 and 18 mGy/cm, respectively. The mean error between the bone models and scanning data from contact measurement was 0.45 mm. The mean error between a 3D model constructed from a dry bone and that constructed from the same bone embedded in a radio-opaque soft tissue substitute was 0.06 mm.

Conclusions 3D bone models constructed from low-radiation dose CT data demonstrated the same level of accuracy as those constructed from normal-radiation dose data. The present simulation system can produce 3D bone models with one-thirtieth of the normal radiation dose in the forearm.

Keywords radiation dose; computed tomography; upper extremity

Introduction

The recent progress in computer technology and development of multidetector computed tomography (CT) has made it possible to use three-dimensional

(3D) preoperative simulations in total arthroplasty, spinal surgery and fracture operation (1–8). We have also developed a simulation system using 3D computer bone models constructed from CT data and demonstrated its clinical feasibility, particularly in upper extremity surgery (9–11). Precise computer bone models are a basic requirement for such systems and previous reports have discussed their accuracy in the lower extremity (12). The accuracy of a computer bone model of the upper extremity, however, has not been elucidated. Another concern about the long-term consequences of CT scanning is radiation exposure to the patient (13–17). Therefore, when using this system in a clinical application, it is essential to set radiation doses of CT at the lowest possible levels while maintaining the accuracy of a bone model. In preoperative simulations of the upper extremity, radiation exposure from CT scanning is expected to be considerably reduced below the normal dose used for diagnostic purposes, particularly because the volume of the extremity is small in comparison to the thorax, abdomen and pelvis. In addition, the contrast between the soft tissue and bone in the extremity is sufficiently distinct to discern the surface of the bone's cortex for constructing a computer bone model.

In the present study, we evaluated the accuracy of computer bone models constructed from CT data of the forearm using our system (9–11) and investigated whether CT scanning with a low radiation dose could effectively preserve the accuracy of a bone model.

Materials and Methods

Data acquisition

Twelve cadaveric dry forearm bones (six radii and six ulnae; Natural Human Bone, Sawbones®, Pacific Research Laboratories Inc., Vashon, WA, USA) were prepared for this study. CT scanning (LightSpeed Ultra16; General Electric, Waukesha, WI, USA) was performed on the bones with 0.625 mm thickness on contiguous slices, with pixels of 0.293 × 0.293 mm under two different conditions: tube voltage, tube current, pitch, and scan time were 120 kV, 50 mA, 0.562 : 1 and 1.0 s for the normal-radiation dose condition (18,19) and 120 kV, 10 mA, 1.750 : 1 and 0.5 s for the low-radiation dose condition, respectively. The values of weighted CT dose index (CTDI), which was the radiation dose for a single rotation of the CT scanner, and dose-length product (DLP), which was calculated by multiplying the CTDI for a scan sequence by the length of coverage along the specimen's length, corresponding to each acquisition protocol, were recorded during CT scanning. The Digital Imaging and Communications in Medicine (DICOM) data for 0.625 mm slices were sent to a workstation for analysis (Dell Precision™ Workstation 650, 266 MHz/2G; Dell Inc., Round Rock, TX, USA).

Construction of bone surface model and accuracy analysis

The bone was segmented, and the 3D surface model was constructed with the threshold CT number set at 150 HU (20). 3D surface generation of the bone cortex was applied (21) using a VTK-based original computer program (Visualization Toolkit, Kitware Inc., Clifton Park, NY, USA). Then, by cancelling the bone marrow data, we completed a surface model of the bone (Figure 1A–C). Thus, 3D surface models of radii and ulnae were constructed in each dose condition (Figure 2A, B). Surface-based registration was performed by independently implementing the iterative closest point algorithm (22,23) with the least-squares method to match the two computer bone surface models constructed under different radiation dose conditions. The error between the two models was then calculated (Figure 2C). The formula to compute errors between the two models is as follows: the point set P with N_p points $\{\overrightarrow{p_i}\}$ from the data shape and model shape X (with N_X supporting geometric primitives: points, lines or triangles) are given. Compute the closest points: $Y_k = C(P_k, X)$, [cost: $0(N_p N_X)$ worst case, $0(N_p \log N_X)$ average]. The mean squared error e_k of that correspondence is given by:

$$e_k = \frac{1}{N_p} \sum_{i=1}^{N_p} \|\overrightarrow{y_{1k}} - \overrightarrow{p_{1k}}\|^2$$

Error between bone surface model and actual bone

Next, the difference between an actual dry bone and its 3D surface model was evaluated. First, the 3D shapes of the bones were measured using a contact-type coordinate-measuring machine (Cyclone, Renishaw, New Mills, UK) (Figure 3A, B), which had an accuracy of <50 μm. The bone measurements were then saved as 2000 points of data (Figure 4A). We defined the 3D points data of the bone surface measured by the contact-type coordinate-measuring machine as the gold standard of accuracy. Surface-based registration was used to match these data points with those of the bone surface model constructed from the CT data under the low-radiation dose condition, and the error between them was calculated (Figure 4B).

Evaluation of soft tissue influence

The final evaluation of the accuracy of the computer bone model was performed by comparing the 3D surface model constructed from the CT data of a dry bone and that constructed from the CT data of a forearm phantom, which was prepared by embedding the same dry bone in a radiation-absorbable soft tissue substitute. This validation procedure was conducted to determine how soft tissue influences the accuracy of the computer bone model. The phantom was prepared by embedding dry bones

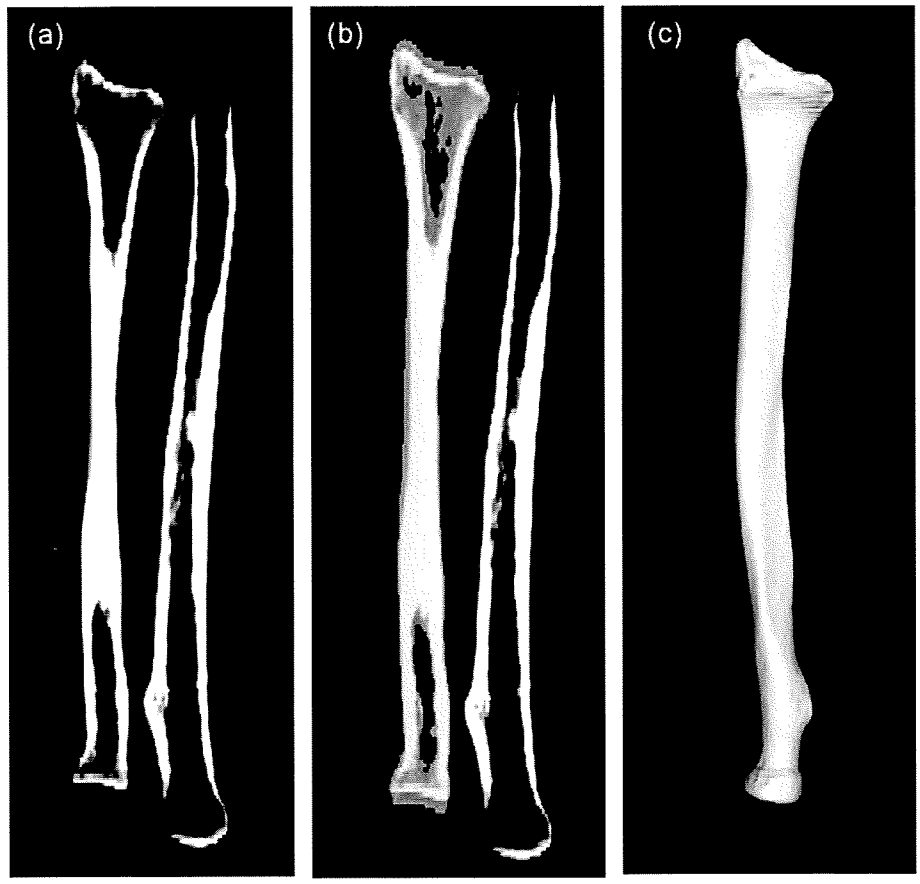

Figure 1. With an image obtained from CT reconstruction (a), the malunited bone was segmented (b) and a 3D surface model was constructed using an original computer program (c)

in a soft tissue substitute made of polyurethane resin and phosphoric acid [$(C_2H_4ClO)_3PO$], which had a CT number of 0 HU (SZ-50; Kyoto Kagaku Co. Ltd., Kyoto, Japan) (24), after scanning the bones with CT. The bones were then re-inspected by CT in the low-radiation dose condition, and the 3D bone model was constructed with a threshold value of 150 HU. Surface-based registration was performed using the computer program with the bone surface models created from the CT data of the forearm phantom and the dry bone to calculate the error between them.

Results

The mean error between the 3D bone surface models constructed under two different CT conditions (i.e. normal- and low-radiation doses) was 0.04 ± 0.01 mm (Table 1). These results indicate that low- and normal-radiation-dose CT parameters provide an almost identical 3D bone surface model. CTDI and DLP with the normal-radiation dose resulted in 9.3 and 563 mGy/cm, respectively. With the low-radiation dose, CTDI and DLP were 0.3 and 18 mGy/cm. The radiation dose of the low-dose condition was about one-thirtieth of the normal-dose condition. The mean error between the 3D bone models constructed from the CT data and scanning data of actual measurements of a bone surface using a contact-type measuring machine was 0.46 ± 0.03 mm (Table 1). The mean error between a 3D surface model constructed from a dry bone and that constructed from a phantom embedded in a radiation-absorbable soft tissue substitute was 0.06 ± 0.01 mm (Table 1).

The 3D bone surface model constructed from low-radiation dose CT data had an accuracy of <0.5 mm, and the influence of soft tissue on the construction of this model was negligible.

Discussion

Although radiation exposure to the human body poses a significant problem (16,17), the benefits of CT as a clinical diagnostic tool and in preoperative surgical planning may outweigh its adverse effects in many situations. With the implementation of 3D bone models constructed from CT data in recent orthopaedic surgeries, the demand for CT has been increasing. They have been used in a simulation–navigation system for implant arthroplasties of the hip and knee joints (25–30). In spinal surgery, CT is used to navigate the placement of pedicle screws (31–34). We also developed a 3D computer simulation system for corrective osteotomy for malunited fractures and reported

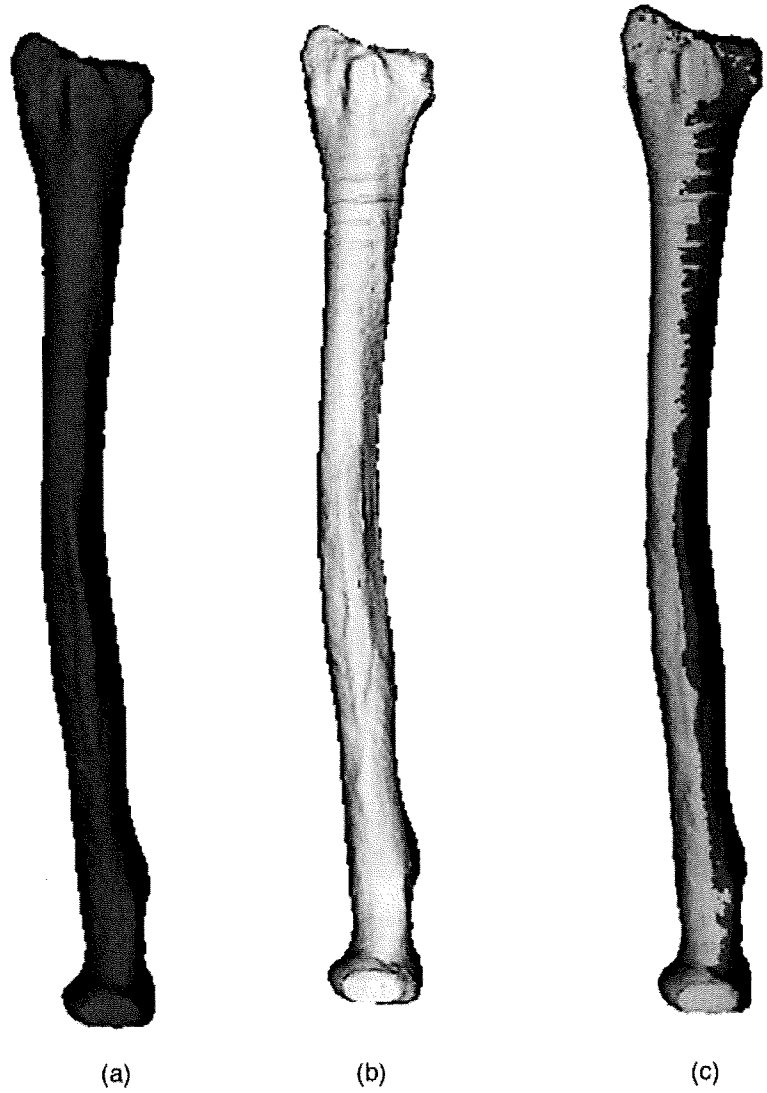

Figure 2. 3D bone surface models constructed from CT data in (a) normal-radiation and (b) low-radiation doses. (a) and (b) were matched to evaluate the error between them (c)

encouraging clinical results in upper extremity cases (10,11).

However, there are two issues to be solved concerning the use of 3D bone models constructed from CT data. The first is the accuracy of a bone model itself. Although accuracy in lower extremity has been reported (12), it has never been clarified in the upper extremity. Therefore, we had first planned to make an error analysis between a 3D bone model and actual measurement of the forearm bone. The other concern is the radiation exposure during CT scanning. When considering the accuracy of a computer bone model, it is also desirable to use as little radiation as possible in order to avoid its adverse effects to the human body. Appropriate CT parameters required for construction of bone models should be specified not only to create a bone model with high accuracy, but also to reduce radiation exposure. Bonel *et al.* (18) investigated the optimal CT parameters to achieve diagnostic image quality with minimum radiation exposure for the wrist and reported that a low tube voltage of 80 kV, a tube current of 100 mA, a thickness of 1.0 mm, a pitch of 1.5 and a rotation time of 0.75 s were adequate. However, if CT is taken for the purpose of creating a 3D bone surface model and not for diagnostic purposes, even less radiation exposure may be adequate because the contrast between the bone and soft tissue is sufficiently distinct. Consequently, we investigated the accuracy of a 3D bone surface model created from CT with a lower radiation dose; CT parameters were set at one-tenth of the tube current, seven-sixths of the pitch and two-thirds of the scan time of clinically established parameters (18). As a result, the radiation exposure from CT scanning with this system was estimated to be as low as one-thirtieth of the standard scanning dose. The 3D bone surface models using low-radiation dose CT parameters were as precise as those using normal-radiation dose CT parameters within 0.5 mm when compared to the actual measurement data, and were thought accurate enough to be used in preoperative simulation and navigation surgeries (20,35–38). The results of the current study also demonstrated that the influence of soft tissue on 3D bone surface models was negligible. The CT number

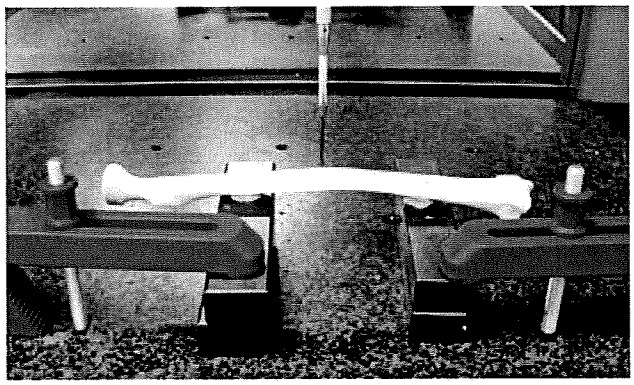

(a)

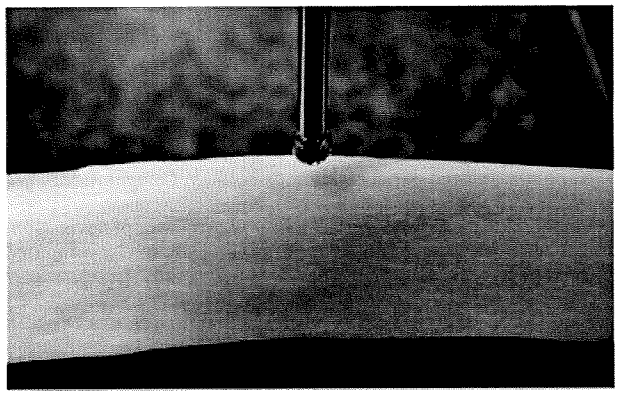

(b)

Figure 3. The contact-type coordinate-measuring machine used to scan the surface of the radius with a probe to create digital 3D models represented by a number of data points (a, b)

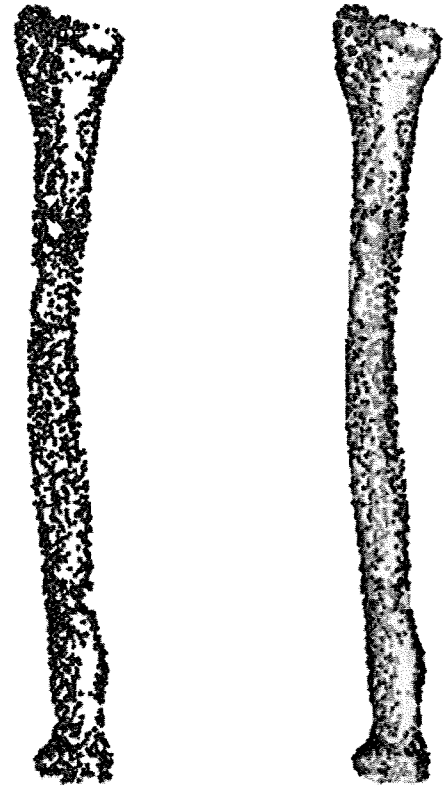

(a) (b)

Figure 4. Data points of bone surface of a radius measured by a coordinate measuring machine (a). The data points and the 3D bone surface model constructed with low-radiation dose were matched (b)

of bone cortex is significantly higher (1000 HU) when compared to soft tissues such as muscle (30–60 HU), blood (50 HU) and fat (−100 HU). This increased CT number allows the contour line of the bone cortex to be clearly recognized without noise when binarization is performed at a threshold value of 150 HU. In addition, the forearm requires less radiation to acquire adequate image quality, since it has a smaller volume compared to that of the thorax, pelvis, femur and tibia.

In this study, the interference posed by the spine and pelvis, which could influence the image quality of the forearm during the actual scanning, was not taken into account. However, their influence was considered negligible so long as the patient was in a prone position and the forearm was elevated over the head during scanning.

Considering these results, we conclude that low-radiation CT scan parameters will be well tolerated, and the bone surface model obtained from it is sufficiently accurate for clinical use.

Table 1. Error of 3D bone models in each condition (mm)

No.	Bone	Error between bone models constructed from: 3D computer model and point data	Normal and low-dose CT scanning	CT data of dry bone and phantom*
1		0.41	0.05	0.05
2		0.42	0.05	0.05
3	Radius	0.43	0.04	0.05
4		0.43	0.03	0.06
5		0.44	0.05	0.06
6		0.49	0.04	0.06
7		0.47	0.06	0.07
8		0.47	0.04	0.08
9	Ulna	0.49	0.05	0.07
10		0.46	0.04	0.07
11		0.46	0.04	0.05
12		0.49	0.04	0.07
Average		0.46 ± 0.03	0.04 ± 0.01	0.06 ± 0.01

*A phantom was prepared by embedding the same dry bone in a radiation absorbable soft tissue substitute.

Acknowledgement

The authors acknowledge the assistance of computer programmer Ryoji Nakao of the Department of Orthopaedic Surgery, Osaka University Graduate School of Medicine, during parts of the experimental procedure.

References

1. Athwal GS, Ellis RE, Small CF, *et al.* Computer-assisted distal radius osteotomy. *J Hand Surg [Am]* 2003; **28**(6): 951–958.

2. Beckmann J, Goetz J, Baethis H, *et al.* Precision of computer-assisted core decompression drilling of the femoral head. *Arch Orthop Trauma Surg* 2006; **126**(6): 374–379.
3. Chen E, Goertz W, Lill CA. Implant position calculation for acetabular cup placement considering pelvic lateral tilt and inclination. *Comput Aided Surg* 2006; **11**(6): 309–316.
4. Ellis RE, Tso CY, Rudan JF, *et al.* A surgical planning and guidance system for high tibial osteotomy. *Comput Aided Surg* 1999; **4**(5): 264–274.
5. Kanlic EM, Delarosa F, Pirela-Cruz M. Computer assisted orthopaedic surgery – CAOS. *Bosn J Basic Med Sci* 2006; **6**(1): 7–13.
6. Shimizu T, Fujioka F, Gomyo H, *et al.* Three-dimensional starch model for simulation of corrective osteotomy for a complex bone deformity: a case report. *Foot Ankle Int* 2003; **24**(4): 364–367.
7. Wong KC, Kumta SM, Chiu KH, *et al.* Precision tumour resection and reconstruction using image-guided computer navigation. *J Bone Joint Surg Br* 2007; **89**(7): 943–947.
8. Yamazaki M, Akazawa T, Okawa A, *et al.* Usefulness of three-dimensional full-scale modeling of surgery for a giant cell tumor of the cervical spine. *Spinal Cord* 2007; **45**(3): 250–253.
9. Murase T, Moritomo H, Goto A, *et al.* Does three-dimensional computer simulation improve results of scaphoid nonunion surgery? *Clin Orthop Relat Res* 2005; **434**: 143–150.
10. Murase T, Oka K, Moritomo H, *et al.* Three-dimensional corrective osteotomy of malunited fractures of the upper extremity with use of a computer simulation system. *J Bone Joint Surg Am* 2008; **90**: 2375–2389.
11. Oka K, Moritomo H, Goto A, *et al.* Corrective osteotomy for malunited intra-articular fracture of the distal radius using a custom-made surgical guide based on three-dimensional computer simulation: case report. *J Hand Surg [Am]* 2008; **33**(6): 835–840.
12. Gelaude F, Vander Sloten J, Lauwers B. Accuracy assessment of CT-based outer surface femur meshes. *Comput Aided Surg* 2008; **13**(4): 188–199.
13. Hall EJ, Brenner DJ. Cancer risks from diagnostic radiology. *Br J Radiol* 2008; **81**(965): 362–378.
14. Paul JF, Abada HT. Strategies for reduction of radiation dose in cardiac multislice CT. *Eur Radiol* 2007; **17**(8): 2028–2037.
15. Kalra MK, Maher MM, Saini S. Multislice CT: update on radiation and screening. *Eur Radiol* 2003; **13**: (suppl 5): M129–133.
16. Berrington de Gonzalez A, Darby S. Risk of cancer from diagnostic X-rays: estimates for the UK and 14 other countries. *Lancet* 2004; **363**(9406): 345–351.
17. Kalra MK, Maher MM, Toth TL, *et al.* Strategies for CT radiation dose optimization. *Radiology* 2004; **230**(3): 619–628.
18. Bonel HM, Jager L, Frei KA, *et al.* Optimization of MDCT of the wrist to achieve diagnostic image quality with minimum radiation exposure. *AJR Am J Roentgenol* 2005; **185**(3): 647–654.
19. Bush CH, Gillespy T III, Dell PC. High-resolution CT of the wrist: initial experience with scaphoid disorders and surgical fusions. *AJR Am J Roentgenol* 1987; **149**(4): 757–760.
20. Sugano N, Sasama T, Sato Y, *et al.* Accuracy evaluation of surface-based registration methods in a computer navigation system for hip surgery performed through a posterolateral approach. *Comput Aided Surg* 2001; **6**(4): 195–203.
21. Lorensen WE, Cline HE. Marching cubes: a high resolution 3D surface construction algorithm. *Comput Graph* 1987; **21**: 163–169.
22. Besl PJ, Mackay N. A method for registration of 3D shapes. *IEEE Trans Patt Anal* 1992; **14**: 239–256.
23. Audette MA, Ferrie FP, Peters TM. An algorithmic overview of surface registration techniques for medical imaging. *Med Image Anal* 2000; **4**(3): 201–217.
24. Shirotani T. Realistic torso phantom for calibration of *in vivo* transuranic nuclide-counting facilities. *J Nucl Sci Technol* 1988; **25**(11): 875–883.
25. Decking R, Markmann Y, Fuchs J, *et al.* Leg axis after computer-navigated total knee arthroplasty: a prospective randomized trial comparing computer-navigated and manual implantation. *J Arthroplasty* 2005; **20**(3): 282–288.
26. Delp SL, Stulberg SD, Davies B, *et al.* Computer assisted knee replacement. *Clin Orthop Relat Res* 1998; **354**: 49–56.
27. DiGioia AM, Jaramaz B, Blackwell M, *et al.* The Otto Aufranc Award. Image guided navigation system to measure intraoperatively acetabular implant alignment. *Clin Orthop Relat Res* 1998; **355**: 8–22.
28. La Palombara PF, Fadda M, Martelli S, *et al.* Minimally invasive 3D data registration in computer and robot assisted total knee arthroplasty. *Med Biol Eng Comput* 1997; **35**(6): 600–610.
29. Langlotz F, Stucki M, Bachler R, *et al.* The first twelve cases of computer assisted periacetabular osteotomy. *Comput Aided Surg* 1997; **2**(6): 317–326.
30. Ybinger T, Kumpan W, Hoffart HE, *et al.* Accuracy of navigation-assisted acetabular component positioning studied by computed tomography measurements: methods and results. *J Arthroplasty* 2007; **22**(6): 812–817.
31. Amiot LP, Lang K, Putzier M, *et al.* Comparative results between conventional and computer-assisted pedicle screw installation in the thoracic, lumbar, and sacral spine. *Spine* 2000; **25**(5): 606–614.
32. Girardi FP, Cammisa FP Jr, Sandhu HS, *et al.* The placement of lumbar pedicle screws using computerised stereotactic guidance. *J Bone Joint Surg Br* 1999; **81**(5): 825–829.
33. Laine T, Lund T, Ylikoski M, *et al.* Accuracy of pedicle screw insertion with and without computer assistance: a randomised controlled clinical study in 100 consecutive patients. *Eur Spine J* 2000; **9**(3): 235–240.
34. Merloz P, Tonetti J, Pittet L, *et al.* Computer-assisted spine surgery. *Comput Aided Surg* 1998; **3**(6): 297–305.
35. Biant LC, Yeoh K, Walker PM, *et al.* The accuracy of bone resections made during computer navigated total knee replacement. Do we resect what the computer plans we resect? *Knee* 2008; **15**(3): 238–241.
36. Koestler W, Sidler R, Gonzalez Ballester MA, *et al.* A feasibility study of computer-assisted bone graft implantation for tissue-engineered replacement of the human ankle joint. *Comput Aided Surg* 2008; **13**(4): 207–217.
37. Ruppin J, Popovic A, Strauss M, *et al.* Evaluation of the accuracy of three different computer-aided surgery systems in dental implantology: optical tracking vs. stereolithographic splint systems. *Clin Oral Implants Res* 2008; **19**(7): 709–716.
38. Tamura Y, Sugano N, Sasama T, *et al.* Surface-based registration accuracy of CT-based image-guided spine surgery. *Eur Spine J* 2005; **14**(3): 291–297.

ELSEVIER

Bone 41 (2007) 77–86

BONE

www.elsevier.com/locate/bone

Sialylation of cell surface glycoconjugates is essential for osteoclastogenesis

Masahiko Takahata [a,*], Norimasa Iwasaki [a], Hiroaki Nakagawa [b], Yuichiro Abe [a], Takuya Watanabe [b], Manabu Ito [a], Tokifumi Majima [a], Akio Minami [a]

[a] *Department of Orthopaedic Surgery, Hokkaido University Graduate School of Medicine, Kita-15 Nishi-7, Kita-ku, Sapporo 060-8638, Japan*
[b] *Division of Biological Sciences, Graduate School of Science, Hokkaido University, Japan*

Received 17 February 2007; revised 17 March 2007; accepted 20 March 2007
Available online 5 April 2007

Abstract

Sialic acid, which is located at the end of the carbohydrate moiety of cell surface glycoconjugates, is involved in many biologic responses, such as intercellular reactions and virus–cell fusion, especially in hematopoietic cells. Here we provide experimental evidence that the sialic acid of cell surface glycoconjugates has a role in osteoclast differentiation. Lectin histochemical study demonstrated the existence of both alpha (2,3)-linked-sialic acid and alpha (2,6)-linked-sialic acid in mouse bone marrow-derived macrophages and in the RAW264.7 macrophage cell line, which are osteoclast precursors. Flow cytometric analysis of surface lectin staining revealed the kinetics of these sialic acids during osteoclastogenesis: alpha (2,3)-linked-sialic acid was abundantly expressed throughout osteoclastogenesis, whereas alpha (2,6)-linked-sialic acid levels declined at the terminal stage of osteoclast differentiation. To investigate the role of sialic acid in osteoclast differentiation, we performed an osteoclastogenesis assay with or without exogenous sialidase treatment. Desialylated cells formed TRAP-positive mononuclear cells, but did not become multinuclear cells despite the normal expression of osteoclast markers such as cathepsin K, integrin β3, and nuclear factor-ATc1. Flow cytometric analysis also demonstrated that exogenous sialidase effectively removed alpha (2,6)-linked-sialic acid, but only slightly changed the alpha (2,3)-linked-sialic acid content, suggesting that alpha (2,6)-linked-sialic acid might be involved in osteoclast differentiation. Findings from knockdown analysis using small interfering RNA oligonucleotides against alpha 2,6-sialyltransferase support this idea: alpha (2,6)-linked-sialic acid-deficient cells markedly inhibit the formation of multinuclear osteoclasts. Our findings suggest that alpha (2,6)-linked-sialic acid of cell surface glycoconjugates has a role in osteoclast differentiation, possibly via its role in the cell–cell fusion process.

Keywords: Osteoclast; Cell fusion; Sialic acid; Glycoconjugate; Sialidase

Introduction

Osteoclasts are bone-resorbing cells that have a pivotal role in bone remodeling. Osteoclasts are differentiated from hematopoietic precursors of the monocyte/macrophage lineage and form multinuclear giant cells via cell–cell fusion [2,35]. Multinucleation is thought to be an essential step in the structural and functional differentiation of osteoclasts, because mononuclear osteoclasts cannot efficiently resorb bone. Recent studies revealed candidate molecules involved in osteoclast fusion: E-cadherin [17], macrophage fusion receptor [37], terminal high mannose type oligosaccharide-mannose receptor [22], ADAM9 [25], CD98 [33], $P2X_7$ receptor [6], CD9 [11], and dendritic cell-specific transmembrane protein [15,38]. The complex mechanisms that govern cell–cell fusion in osteoclast differentiation, however, are not fully understood.

It is well established that cell fusion is a biologically and pathophysiologically important event in vivo and occurs not only in osteoclasts, but also among foreign body giant cells [18,24], myoblasts [5], sperm and egg [9,26], and virus and cells [32,23]. Among these, cell surface sialic acid is implicated in some fusion mechanisms. The best known fusion mechanism is the sialic acid recognition and binding mechanism in virus–cell fusion. In parainfluenza virus–cell fusion, sialic acid residues of the uninfected host cell surface are recognized by the hemagglutinin of the virus protein, and interactions between these molecules mediate fusion of virus

* Corresponding author. Fax: +81 11 706 6054.
E-mail address: takamasa@med.hokudai.ac.jp (M. Takahata).

8756-3282/$ - see front matter © 2007 Elsevier Inc. All rights reserved.
doi:10.1016/j.bone.2007.03.016

to cells or virus-infected cells to uninfected cells. Moscona et al. demonstrated that desialylated cells are unable to fuse with parainfluenza virus-infected cells [23]. Another sialic acid-related fusion mechanism occurs in sperm–egg fusion. Egg surface sialic acid has a role in triggering the sperm acrosome reaction, an exocytotic event required for membrane fusion of the gametes in sperm–egg fusion [9]. To our knowledge, however, there are no reports of the involvement of cell surface sialic acid in osteoclast fusion.

Sialic acid is also called neuraminic acid, which represents a family of derivatives of C9 sugar that include carboxylic acid, and are components of glycoproteins and glycolipids. In mouse, there are mainly two kinds of sialic acid, *N*-acetylneuraminic acid and *N*-glycolylneuraminic acid. Humans have only *N*-acetylneuraminic acid. Sialylated glycoconjugates are present on many mammalian cell membranes and are implicated in many biologic processes, such as intercellular adhesive reactions, hematopoietic cell differentiation, and virus–cell fusion [4,14,29,31]. The structural diversity, peripheral position of sialic acid on oligosaccharide chains of glycoconjugates, and regulated expression of sialylglycoconjugates appear to correlate with their functions [36]. The surfaces of monocyte/macrophage lineage cells contain sialylated glycoproteins and glycolipids and the functional capacity of these cells changes after the removal of sialic acid from the cell surface glycoconjugates [29]. Because osteoclasts are of the monocyte/macrophage lineage and a lectin-histochemical study of pathologic bone tissue demonstrated the membranous and intracytoplasmic distribution of sialic acids in osteoclasts and osteoclast precursor cells [10], we hypothesized that the sialic acid of cell surface glycoconjugates is involved in osteoclast fusion.

In the present study, we first investigated the change in glycoconjugate sialylation during osteoclast differentiation, and then examined the effect of desialylation of osteoclast precursors on the differentiation of osteoclasts, especially in the cell–cell fusion process.

Materials and methods

Animals and reagents

Male ddY mice (6–9 weeks old) were purchased from Sankyo Laboratories (Tokyo, Japan). The studies using mice were approved by the institutional animal review board. Recombinant human macrophage-colony stimulating factor (rhM-CSF) was purchased from Wako Pure Chemical Industry Co., Ltd. (Osaka, Japan). Soluble recombinant human receptor activator of nuclear factor-κB ligand (sRANKL) was purchased from PeproTech EC, Ltd. (London, U.K.). Sialidase (SAase; provided as neuraminidase from Arthrobacter Ureafaciens) was purchased from Nacalai Tesque, Inc. (Kyoto, Japan). Fluorescein isothiocyanate (FITC)-labeled lectin Arachis hypogaea (PNA), Maackia amurensis (MAA), and Sambucus nigra (SNA-I) were purchased from EY Laboratories (San Mateo, CA). All the antibodies used in this study were purchased from Cell Signaling (Beverly, MA).

Osteoclastogenesis assay

Osteoclast differentiation from bone marrow cells was achieved as previously described with slight modification [34]. Briefly, femurs and tibias of adult mice were aseptically removed and dissected free of adhering tissues. The bone ends were cut off with scissors and the marrow cavity was flushed with α-minimum essential medium (α-MEM). The marrow cells were collected, washed with α-MEM, and red blood cells were removed by treatment with 0.727% NH4Cl-0.017% Tris–Cl (pH7.2)-phosphate-buffered saline (PBS) solution. After washing, cells were cultured in α-MEM containing 10% fetal bovine serum (FBS), 100 IU/ml penicillin G (Meiji Seika, Tokyo, Japan), 100 μg/ml streptomycin (Meiji Seika), and rhM-CSF (30 ng/ml) at 5×10^6 cells in a 10-cm suspension culture dish (Corning Costar Inc., Corning, NY). After 3-day culture, cells were washed vigorously with PBS twice to remove nonadherent cells and bone marrow macrophage cells (BMMs) were harvested by pipetting with 0.02% EDTA in PBS. BMMs were resuspended in the α-MEM containing 10% FBS, 30 ng/ml rhM-CSF, and 100 ng/ml sRANKL, and cultured on 48-well plates (1×10^5 cells/well). Cells were incubated for 3 days at 37 °C in a 5% humidified CO_2 incubator.

The osteoclastogenic differentiation of the murine monocyte/macrophage cell line RAW264.7 was achieved by seeding the cells at a density of 1×10^4 cells/well in 48-well plates and culturing for 5 days with 50 ng/ml sRANKL in Dulbecco's MEM (DMEM) containing 10% FBS.

Lectin histochemical analysis

Cells were cultured on glass coverslips and fixed for 5 min with 4% paraformaldehyde and then treated with 0.1% Triton X-100 to permeate the cell membrane. After blocking with 1% bovine serum albumin, cells were incubated with FITC-labeled MAA lectin or FITC-labeled SNA-I lectin, and reacted with 4′,6-diamidino-2-phenylindole, dihydrochloride (Dojindo Laboratories, Japan), and phalloidin-tetramethyl isothiocyanate (Sigma Chemical Co., St. Louis, MO, P1951) to identify nuclei and F-actin. MAA binds to alpha (2,3)-linked-sialic acid and SNA-I binds to alpha (2,6)-linked-sialic acid, respectively. Cells were then mounted on glass slides and examined with a confocal laser-scanning microscope (Fluoview FV300, Olympus).

Treatment of osteoclast precursor cells with exogenous SAase

To evaluate the role of cell surface sialic acid in the osteoclast differentiation process, cell surface glycoconjugates were desialylated by exogenous SAase. In an osteoclastogenesis assay, cells were exposed to either SAase (100 mU/ml, 10 mU/ml, 1 mU/ml, or 0 mU/ml) or heat-inactivated SAase (100 mU/ml).

Removal of sialic acid from the plasma membrane was ascertained as described by Stamatos et al. [29]. Cells were desialylated with 100 mU/ml SAase for 3 h in a moist chamber, and then treated with FITC-labeled lectin PNA and analyzed by fluorescent microscopy and flow cytometry. PNA binds to the galactose moiety that is exposed on cell surface glycoconjugates after removal of the terminal sialic acid. For flow-cytometry, mock- and SAase-treated cells (2×10^5) were suspended in 0.1 ml PBS, pH 7.4, containing 2% FBS, and incubated with 10 μg/ml FITC-labeled PNA or left unstained. Cells were incubated with PNA for 45 min at 4 °C before unbound lectin was removed by washing the cells at 4 °C with 2 ml PBS, pH 7.4, containing 2% bovine serum albumin. Cells were fixed in 1% paraformaldehyde and analyzed by flow cytometry using a Becton Dickinson FACS Caliber (Becton Dickinson, Franklin Lakes, NJ). Data were analyzed using CELL Quest data analysis software (Becton Dickinson).

Kinetics of sialic acid expression on plasma membranes during osteoclastogenesis

To analyze the kinetics of sialic acid expression on plasma membranes during osteoclastogenesis with or without SAase treatment, we quantitatively investigated the alpha (2,3)-linked-sialic acid and alpha (2,6)-linked-sialic acid content by flow cytometry. We prepared four different conditioned RAW 264.7 cells cultured with DMEM and 10% FBS: (1) no treatment, (2) desialylated with 100 mU/ml SAase for 3 h, (3) cultured with sRANKL (50 ng/ml) for 4 days, and (4) desialylated with 100 mU/ml SAase and cultured with sRANKL (50 ng/ml) for 4 days. These cells were treated with FITC-labeled lectin MAA (50 μg/ml) or FITC-labeled lectin SNA-I (50 μg/ml) and analyzed by flow cytometry as described above.

Tartrate-resistant acid phosphatase (TRAP) staining and TRAP activity measurement

Osteoclast generation was confirmed by TRAP staining. After aspiration of medium, cells were fixed with 1% glutaraldehyde in PBS for 5 min at room temperature and stained for TRAP using a histochemical kit (Hokudo, Co, Ltd. Japan) according to the manufacturer's instructions. Mature osteoclasts were identified microscopically as TRAP-positive cells with at least three nuclei and the number of cells was quantified for each well.

TRAP activity of the cell culture supernatant was measured using a TRAP activity assay kit according to the manufacturer's protocol (Hokudo, Co, Ltd.). Briefly, 30 μl of cell culture supernatant was retrieved and mixed with TRAP staining solution in 96-well plates. The plates were incubated in a moist chamber at 37 °C for 3 h and the absorbance of the solution was measured at 540 nm.

Resorption pit assay

Osteoclasts were further characterized by assessing their ability to form resorption pits on dentin slices. Dentin slices were purchased from Hokudo, Co., Ltd. The slices were placed in 48-well plates and BMM cells were seeded into each well with α-MEM containing 10% FBS, 30 ng/ml rhM-CSF, and 100 ng/ml sRANKL. After 10-day culture with or without SAase treatment, dentin slices were sonicated in 1 M ammonia solution to remove the cells and stained with hematoxylin. The area of resorption lacunae (pits) on each slice was measured and analyzed with Image J software (http://rsb.info.nih.gov/nih-image/).

Real-time polymerase chain reaction (PCR) quantification of gene expression

Total RNA from cultured cells was isolated using the Qiagen RNeasy Mini Kit according to the manufacturer's instructions (Qiagen, Valencia, CA). cDNA were synthesized from 1 μg total RNA using reverse transcriptase and oligo-dT primers in a volume of 10 μl, and the reaction mixture was adjusted to 50 μl with TE buffer (10 mM Tris–1 mM EDTA, pH 8.0) for PCR analysis. PCR was performed and monitored using the DNA Engine Opticon 2 System (MJ Research, Hercules, CA). The 2× SYBR Green Mastermix (DyNAmo™ HS SYBR Green qPCR Kit) was based on a hot start version of a modified Thermus brockianus DNA polymerase (Finnzymes Oy, Finland). cDNA samples (5 μl for a total volume of 20 μl per reaction) were analyzed for both the genes of interest and the reference genes (glyceraldehyde-3-phosphate dehydrogenase; GAPDH). Primer sequences used for mouse beta galactoside alpha (2,3) sialyltransferase-I, -II, -III, -IV, V (ST3Gal-I, II, III, IV, V), and beta galactoside alpha (2,6) sialyltransferase-I, -II (ST6Gal-I, -II), calcitonin receptor, cathepsin K, integrin β3, nuclear factor of activated T cells c1 (NF-ATc1), and GAPDH are shown in Table 1. Cycle threshold (Ct) values were obtained graphically. Relative expression was calculated using the comparative Ct method. Samples were normalized for the expression of GAPDH by calculating the ΔCt (Ct gene of interest − Ct GAPDH); subsequently, the ΔΔCt values were calculated by ΔCt sample − ΔCt calibrator, where the calibrator is the control sample (unstimulated BMMs). Relative expression of the different genes is expressed as $2-(\Delta Ct)$.

Small interfering RNA (SiRNA)

Three duplexed Stealth™ siRNAs designed against the ST6Gal-I (accession no. NM_145933) were purchased from Invitrogen (Carlsbad, CA): MSS237905, sense 5′-AUAAUGAUGAUACCCAGCAUGCCGG-3′, antisense 5′-CCGGCAUGCUGGGUAUCAUCAUUAU-3′; MSS237906, sense 5′-UUAUCAAUCUCUCGACCCAGCUGGG-3′, antisense 5′-CCCAGCUGGGUCGAGAGAUUGAUAA-3′; MS237907, sense 5′-AAGACACGACGGCACACUUAUGCCA-3′, antisense 5′-UGGCAUAAGUGUGCCGUCGUGUCUU-3′. Transfection efficacy was analyzed using 50 nM BLOCK-iT™ Alexa Fluor® Red Fluorescent Oligo (Invitrogen). Preliminary experiments indicated that siRNA MS237907 most efficiently downregulated the ST3Gal-I mRNA expression in RANKL-stimulated RAW 264.7 cells.

To investigate the role of ST6Gal-I in osteoclast differentiation, RANKL-stimulated RAW 264.7 cells in 48-well plates were transfected using either 50 nM siRNA control (Stealth RNAi negative control, Invitrogen) or siRNA MS209002 combined with 0.8 μl Lipofectamine RNAiMax (Invitrogen) in Opti-MEM media supplemented with sRANKL on day 1 of differentiation. Media were replaced every 2 days after RANKL stimulation by DMEM with 10% FBS and sRANKL. No antibiotics were used. The cells were incubated for 4 days (72 h after transfection) at 37 °C in a CO2 incubator, after which they were fixed in 1% glutaraldehyde in PBS. TRAP staining was performed to confirm the presence of TRAP-positive multinuclear cells (MNCs).

Statistical analysis

Results are shown as the mean ± SD of at least three experiments. Data were statistically analyzed using one factor analysis of variance followed by Bonferroni/Dunn test as a post hoc analysis for the osteoclast formation assay. For the bone resorption assay and siRNA knock down assay, statistical analysis was performed using Student's *t*-test. A P value of less than 0.05 was considered to be statistically significant.

Results

Expression of sialic acid in osteoclast precursor cells and osteoclasts

First, we confirmed the existence of alpha (2,3)-linked-sialic acid stained with MAA lectin and alpha (2,6)-linked-sialic acid stained with SNA-I lectin in osteoclast precursors by lectin histochemical study (Fig. 1). In BMMs, both alpha (2,3)-linked-sialic acid and alpha (2,6)-linked-sialic acid were distributed in the paranuclear area and cytoplasm. After 3-day culture in the

Table 1
Sequence of primers used in quantitative RT-PCR

Gene	Forward primers (5′–3′)	Reverse primers (5′–3′)	Amplicon (bp)	Accession number
ST3Gal-I	CCA ACA ACC TGA GCG ACA	TCC TAC AAC TGC ACA GCG TC	110	NM_009177
ST3Gal-II	AAG TGC TCT CTT CGG GTG TG	GCT GTG GTG CGA GTA GGT G	87	BC066064
ST3Gal-III	AGC CAC CAA GTA CGC AAA CT	CCT AGC CCA CTT GCG AAA G	136	NM_009176
ST3Gal-IV	CGA CGT GGT CAT CAG ATT GA	GGG CCG ACT CAG GAT AGA AG	98	NM_009178
ST3Gal-V	GTG GAC CCT GAC CGG ATA AA	CAT AGC CGT CTT CGC GTA CC	90	NM_011375
ST6Gal-I	CTG GGC CTT GGC ATA AGT G	AAA CCT CAG GAC CGC ATC AT	101	NM_145933
ST6Gal-II	GGA GAC ATC ATG GCG ATC A	CAT GTC GCT GTC ATA GGC TT	97	NM_172829
CTR	TGG CTG TGT TTA CCG ACG AG	CGA GTG ATG GCG TGG ATA AT	146	NM_007588
Cathepsin K	TGGATGAAATCTCTCGGCGT	TCATGTCTCCCAAGTGGTTC	123	NM_007802
Int ß3	TGACTCGGACTGGACTGGCTA	CACTCAGGCTCTTCCACCACA	414	NM_016780
NF-ATc1	CCT GGA GAT CCC GTT GC	GGT GTT CTT CCT CCC GAT GT	135	AF239169
GAPDH	ACTTTGTCAAGCTCATTTCC	TGCAGCGAACTTTATTGATG	269	BC098095

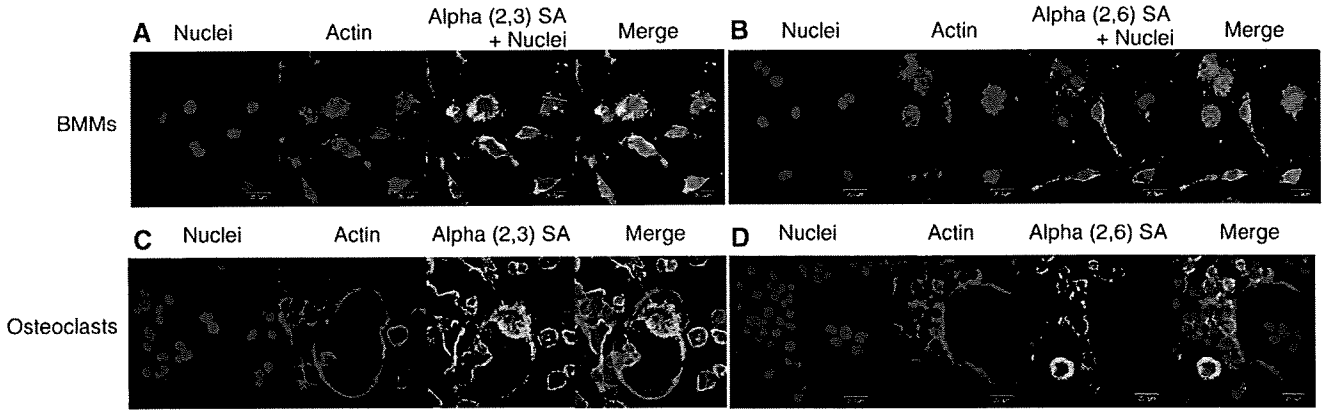

Fig. 1. Immunohistochemical study of the alpha (2,3)-linked sialic acid (alpha (2,3) SA) stained with MAA lectin and alpha (2,6)-linked-sialic acid (alpha (2,6)-SA) stained with SNA-I lectin in BMM and osteoclasts. Nuclei were stained with DAPI and actin was stained with phalloidin-TRITC. (A, C) Alpha (2,3)-SA is expressed in BMM, and after 3-day culture in the presence of rhM-CSF and sRANKL, alpha (2,3)-SA accumulated on the plasma membrane in pre-fusion mononuclear cells. Alpha (2,3)-SA is also expressed in the paranuclear area and the area consistent with the actin ring in polykaryocytes. (B, D) Alpha (2,6)-SA is expressed in BMMs, and accumulates on the cell surface of pre-fusion mononuclear cells, whereas it is markedly decreased in the cells in which cell fusion was complete with actin ring formation.

presence of rhM-CSF and sRANKL, mononuclear cells undergoing cell fusion accumulated both alpha (2,3)-linked-sialic acid and alpha (2,6)-linked-sialic acid on the plasma membrane. In multinuclear giant cells with actin ring formation, alpha (2,3)-linked-sialic acid was still expressed in the paranuclear area and along the actin ring, whereas the expression of alpha (2,6)-linked-sialic acid was degraded in polykaryocytes.

To gain insight into the mechanisms underlying changes in the expression of alpha (2,3)-linked and alpha (2,6)-linked sialic acids during osteoclastogenesis, we investigated the alterations in mRNA expression of the known cloned sialyltransferases (ST3Gal-I, II, III, IV, V, and ST6Gal-I, II) before and after RANKL stimulation (Fig. 2). Of those sialyltransferases, the results of real-time RT-PCR analysis showed that all five beta galactoside alpha (2,3)-sialyltransferases were expressed in BMMs, whereas only ST6Gal-I was expressed in two of the beta galactoside alpha (2,6)-sialyltransferases. mRNA expression of ST3Gal-I and ST3Gal-V changed significantly after RANKL stimulation.

Most of the potential sialylation sites of accessible glycoconjugates on the osteoclast precursor surface are sialylated

BMMs stimulated with rhM-CSF and sRANKL for 1 day were desialylated with exogenous SAase and removal of sialic acid from cell surface glycoconjugates was confirmed by PNA lectin staining that bound specifically to the exposed penultimate galactose residue of desialylated cell surface glycoconjugates (Figs. 3A–D). FITC-labeled PNA bound to the surface of mock-treated BMM, yielding a mean channel fluorescence of 18 (Fig. 3E, dotted line), which was approximately 4-fold greater than the fluorescence of unstained mock-treated cells (Fig. 3E, black area). After BMMs were treated with 100 mU/ml SAase for 3 h, there was a greater than 31-fold increase in the amount of PNA that bound to the cell surface (mean channel fluorescence, 123; Fig. 3E, gray area). Thus, at least 88% of potential sialylation sites on cell surface glycoconjugates that were accessible to exogenous SAase were sialylated in BMMs.

Desialylation of osteoclast precursor cells inhibits RANKL-induced MNC formation during osteoclastogenesis

SAase treatment inhibited rhM-CSF and RANKL-induced osteoclast differentiation from BMMs to TRAP-positive multinuclear osteoclasts in a dose-dependent manner (Figs. 4A–I). SAase concentrations of 10 mU/ml more significantly reduced the formation of multinuclear mature osteoclasts compared to mock-treated cells. Morphologically, BMMs that were spindle-shaped on the culture dish at Day 1 became small round mononuclear cells at Day 2. During this 2-day period, there was no apparent difference between mock-treated cells and SAase treated cells. After 3-day culture, TRAP-positive MNCs were formed in mock-treated and heat-inactivated SAase-treated cells, whereas there was a small number of TRAP-positive MNCs in SAase-treated cell cultures. In SAase-treated cell culture, there were TRAP-positive mononuclear cells. TRAP activity of the cell culture supernatant increased after rhM-CSF and sRANKL stimulation, and the TRAP activity value was significantly lower in SAase-treated cells compared to mock-treated cells (Fig. 4J).

To investigate the bone resorbing ability of osteoclasts differentiated from desialylated BMMs, the resorption pit areas of dentin slices were measured after 10-day culture with or without SAase treatment (Fig. 4L). The resorption pit area in 100 mU/ml SAase-treated cells was 8.7±2.9%, significantly smaller than the area of 42.9±7.9% in mock-treated cells. The resorption pit size was comparatively small with no continuity in 100 mU/ml SAase-treated cells.

A similar inhibitory effect of SAase treatment on osteoclast differentiation was observed in sRANKL-induced osteoclastogenesis of RAW 264.7 cells (Figs. 4M, N). The number of TRAP-positive MNCs in 100 mU/ml SAase-treated cells decreased significantly. There was no significant difference

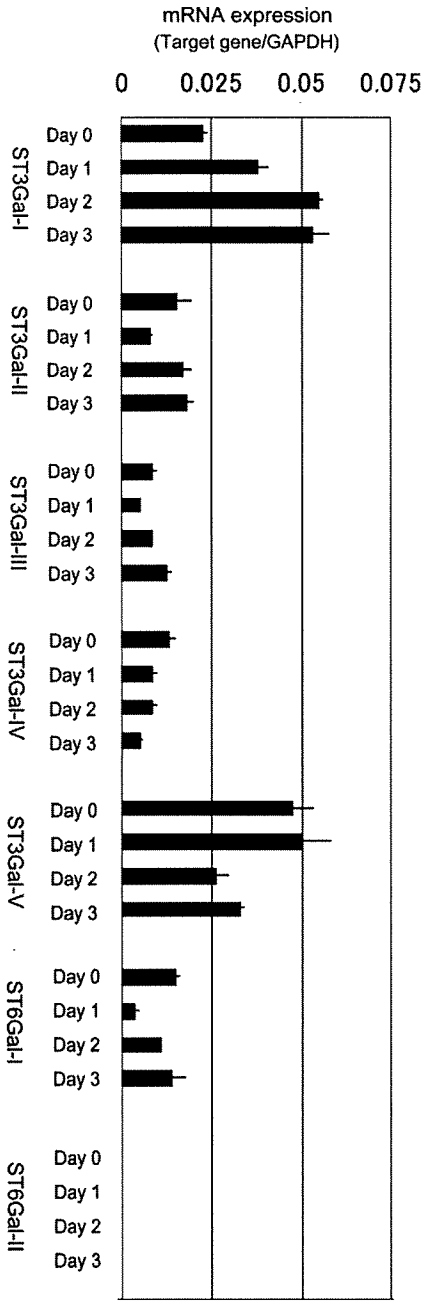

Fig. 2. Quantitative real-time RT-PCR analysis. mRNA expression of sialyltransferases during osteoclastogenesis. BMMs were cultured in the presence of rhM-CSF (30 ng/ml) and sRANKL (100 ng/ml). The mean and SD of three examinations are shown. ST3Gal-I, II, III, IV, V (mouse beta galactoside alpha 2,3 sialyltransferase-I, -II, -III, -IV, -V), and ST6Gal-I, -II (beta galactoside alpha 2,6 sialyltransferase-I, -II).

between mock-treated and 1 to 10-mU/ml SAase-treated cells in the number of TRAP-positive MNCs, but the size of the cells and the number of nuclei in the osteoclasts in the mock-treated group were obviously larger than those in the SAase-treated cells.

Effects of desialylation of cell surface glycoconjugates on osteoclast-related gene expression

To gain insight into the effect of desialylation of osteoclast precursor cells on osteoclast differentiation, mRNA expression levels of osteoclast-related genes induced during osteoclastogenesis were investigated by quantitative real-time RT-PCR (Fig. 4K). The calcitonin receptor, cathepsin K, integrin β3, and NF-ATc1 genes were induced during the first 2 day with a similar trend in both mock-treated and SAase-treated cells. SAase treatment blocked mRNA expression of the calcitonin receptor and NFATc1 at day 3, but did not affect the expression of cathepsin K and integrin β3 throughout the entire differentiation period.

Kinetics of sialic acid expression on plasma membranes during osteoclastogenesis

Flow cytometric analysis of surface lectin staining showed the change in cell surface sialic acid content during osteoclastogenesis (Fig. 5). Alpha (2,3)-linked sialic acid was highly expressed on the surface of these osteoclast precursor cells, and was still expressed at day 4 after sRANKL stimulation. Alpha (2,6)-linked-sialic acid was also detected in the osteoclast precursor cells, whereas its expression markedly decreased in half of the cells at day 4 after sRANKL stimulation (Fig. 5G). At day 4 after RANKL stimulation, there were cells in various stages, including pre-fusion osteoclasts and cells that had completed cell fusion. This means that only the alpha (2,6)-linked-sialic acid content was significantly reduced with osteoclast differentiation.

We also investigated the change in sialic acid content before and after SAase digestion (Figs. 5B, D, F, H). The exogenous SAase slightly changed the alpha (2,3)-linked-sialic acid content, whereas it effectively removed alpha (2,6)-linked-sialic acid. These findings indicate that SAase can easily access alpha (2,6)-linked-sialic acid, but cannot access alpha (2,3)-linked-sialic acid on the surface of osteoclast precursor cells.

Knockdown of ST6Gal-I with siRNA

Because the inhibitory effects of SAase treatment on osteoclast differentiation are considered to derive from the removal of alpha (2,6)-linked-sialic acid, we further characterized the role of alpha (2,6)-linked-sialic acid in osteoclast differentiation using ST6Gal-I knockdown cells. Preliminary studies showed that the mean transfection efficiency was 70% to 80% of the total cells at 48 h after transfection, based on the uptake of a fluorescent double-stranded oligomer. Among the three siRNAs against targets in ST6Gal-I, siRNA MS237907 most effectively downregulated ST6Gal-I mRNA expression (Fig. 6).

In the osteoclastogenesis assay, cells were transfected with MS237907 or control siRNAs at 1 day after sRANKL stimulation and examined 72 h after transfection. Cells transfected with control siRNA showed TRAP-positive multinuclear giant cell formation (Fig. 6B). In contrast, TRAP-positive multinuclear giant cells were rarely observed in ST6Gal-I knockdown cells.

Discussion

The results of the present study suggest that sialylation of cell surface glycoconjugates has an important role in osteoclast differentiation. Sialic acid is expressed in osteoclast precursors,

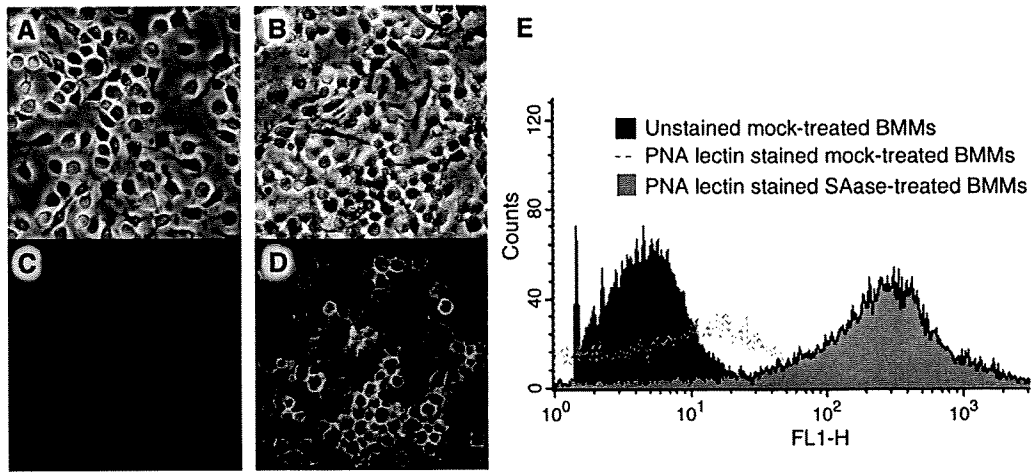

Fig. 3. PNA lectin staining of osteoclast precursor cells with or without SAase treatment. PNA binds to the galactose moiety that is exposed on cell surface glycoconjugates after the removal of the terminal sialic acid. (A, C) Mock-treated BMMs. (B, D) SAase-treated BMMs. (C, D) FITC-PNA lectin staining. (E) FACs analysis of BMMs.

and subsequently accumulates on the cell surface after RANKL stimulation. Interestingly, removal of sialic acid from cell surface glycoconjugates appeared to strongly inhibit osteoclast differentiation, suggesting that cell surface sialic acid is involved in osteoclast differentiation. Furthermore, the findings that desialylated osteoclast precursor cells formed TRAP-positive mononuclear cells, but MNC formation in both BMMs and RAW 264.7 cell lines was inhibited, indicate that sialic acid is involved in the osteoclast fusion process. Considering the fact that sialic acid is implicated in cell–cell adhesive reactions, especially in hematopoietic cells [4,27,8,13], both in ligand-promoting interactions in virus–cell fusion and in selectin-mediated cell–cell adhesion, it is reasonable to suppose that the sialic acid of osteoclast precursor cells mediates cell–cell fusion during osteoclast differentiation.

Among several structurally diverse sialylated glycoconjugates, the results of this study suggest that alpha (2,6) linked-sialic acid is probably the most important for osteoclast cell–cell fusion. As an interesting result of the sialic acid study, alpha (2,6)-linked-sialic acid, which is expressed on the surface of pre-fusion mononuclear cells, markedly decreased once the cells completed fusion to polykaryocytes, suggesting that alpha (2,6)-linked-sialic acid might be involved in the cell–cell fusion process. Because our flow cytometric analysis of surface lectin staining demonstrated that the exogenous SAase effectively removed alpha (2,6)-linked-sialic acid but only slightly changed the alpha (2,3)-linked-sialic acid content, the inhibitory effect of SAase treatment on osteoclast differentiation is considered to derive from the deficiency of alpha (2,6)-linked-sialic acid. The reason for the discrepancy in the efficacy of SAase to remove structurally diverse sialylated glycoconjugates might be that most of the alpha (2,6)-linked-sialic acid is accessible to the exogenous SAase, but alpha (2,3)-linked-sialic acid is not accessible to it because of the conformational structure of sialylglycoconjugates. Furthermore, the fact that ST6Gal-I knockdown cells markedly reduced the ability to form TRAP-positive MNC, supports the idea that alpha (2,6)-linked-sialic acid on the osteoclast precursor cells might be responsible for osteoclast maturation, possibly via its role in the cell–cell fusion process.

Although the mechanism by which sialic acid mediates osteoclast cell–cell fusion remains unclear, there are some candidate molecules or mechanisms based on previous studies of sialic acid. One is a lectin-associated protein such as the macrophage-restricted plasma membrane receptor known as sialoadhesin. Sialoadhesin is a prototypic member of the Siglec family of sialic acid binding immunoglobulin-like lectins that is expressed in subpopulations of macrophages, including bone marrow and inflammatory macrophages [27,8]; however, this molecule mediates cell–cell adhesion via recognition of a particular alpha (2,3)-linked-sialic acid and its expression is decreased with osteoclast differentiation (data not shown). Sialylation of integrin also affects the binding capacity of integrin. In the differentiation of myeloid cells along the monocyte/macrophage lineage, β_1 integrin is hyposialylated with the downregulation of ST6Gal-I expression, leading to enhanced adhesion to fibronectin [28]. Consequently, sialylation of integrins or other adhesive molecules that are expressed in osteoclast precursors, might modulate the function of these adhesive molecules. A negatively charged compound of sialic acid or an acidic condition generated by the sialylation of cell surface glycoconjugates might also affect cell–cell fusion because pH changes modulate osteoclast differentiation and activity [19].

Another possible mechanism of inhibition of osteoclast differentiation by SAase treatment is the interference of rhM-CSF or RANKL signaling because sugar chains of membranous receptor proteins sometimes affect the function of signal transmission [3,14,20]. Membrane lipid rafts, which are mainly composed of gangliosides that contain sialic acid, have a crucial role in receptor activation of nuclear factor-κB and Akt signaling in osteoclast differentiation [7,12]. Also, sialylation of cell surface glycoconjugates influences the function of the tissue necrosis factor receptor [14,31]. RANK expressed on